Topological surface Fermi arcs in the magnetic Weyl semimetal $Co_3Sn_2S_2$

Qiunan Xu,[1] Enke Liu,[1,2] Wujun Shi,[1,3] Lukas Muechler,[4] Jacob Gayles,[1] Claudia Felser,[1] and Yan Sun[1,*]

[1]*Max Planck Institute for Chemical Physics of Solids, Dresden 01187, Germany*

[2]*Institute of Physics, Chinese Academy of Sciences, Beijing 100190, China*

[3]*School of Physical Science and Technology, ShanghaiTech University, Shanghai 200031, China*

[4]*Department of Chemistry, Princeton University, Princeton, New Jersey 08544, USA*

Very recently, the half-metallic compound $Co_3Sn_2S_2$ was proposed to be a magnetic Weyl semimetal (WSM) with Weyl points only 60 meV above the Fermi level E_F. Owing to the low charge carrier density and large Berry curvature induced, $Co_3Sn_2S_2$ possesses both a large anomalous Hall conductivity and a large anomalous Hall angle, which provide strong evidence for the existence of Weyl points in $Co_3Sn_2S_2$. In this work, we theoretically study the surface topological feature of $Co_3Sn_2S_2$ and its counterpart $Co_3Sn_2Se_2$. By cleaving the sample at the weak Sn-S/Se bonds, one can achieve two different surfaces terminated with Sn and S/Se atoms, respectively. The resulting Fermi-arc-related states can range from the energy of the Weyl points to $E_F - 0.1$ eV in the Sn-terminated surface. Therefore, it should be possible to observe the Fermi arcs in angle-resolved photoemission spectroscopy (ARPES) measurements. Furthermore, in order to simulate quasiparticle interference in scanning tunneling microscopy (STM) measurements, we also calculate the joint density of states for both terminals. This work should be helpful for a comprehensive understanding of the topological properties of these two magnetic WSMs and further ARPES and STM measurements.

I. INTRODUCTION

Following the discovery of topological insulators (TIs) [1,2], topological band theory was successfully applied to metals, revealing a number of different topological semimetallic states [3–10]. These topological semimetals can be classified according to the particular details of their electronic band structure, and Weyl semimetals (WSMs) are one of the most extensively studied cases of these classes. In Weyl semimetals, the conduction and valence bands cross linearly in momentum space via doubly degenerate Weyl points, which behave as monopoles of Berry curvature with positive or negative chirality. In order to avoid the divergence of Berry curvature in momentum space, the Weyl points must appear in pairs with opposite chiralities, and the only way to annihilate this pair of Weyl points is to move them to the same k point. Because of the existence of these Weyl points, WSMs can host several exotic transport properties in bulk, such as the chiral anomaly effect [11–14], gravitational anomaly effect [15], and strong intrinsic anomalous Hall and spin Hall effects [16–18], and exhibit a large magnetoresistance [11–13,19–22]. Moreover, like TIs, WSMs also possess topologically protected surface states. Owing to the net Berry flux between Weyl points with opposite chiralities, the surface states in WSMs present as nonclosed Fermi arcs terminating at two opposite Weyl points [3]. Such Fermi arcs are different from the surface states in TIs and other topological materials, where the Fermi surfaces (FSs) present as closed curves at a fixed energy. As a result, the Fermi arc state plays the role of a fingerprint for WSMs and

provides the most direct way to verify the existence of Weyl points that can be measured by surface detection techniques, such as angle-resolved photoemission spectroscopy (ARPES) and scanning tunneling microscopy (STM).

The existence of Weyl points requires lifting the spin degeneracy of the system by breaking the inversion or time-reversal symmetry (or both). To date, many WSMs with the broken inversion symmetry have been theoretically predicted, and some have been experimentally verified, including the type-I WSM state in noncentrosymmetric transition-metal monophosphides (Ta/Nb)(As/P) [11–14,23–33] and the type-II WSM state in WTe_2 and $MoTe_2$ [34–39]. In contrast, there are only a few candidates for magnetic WSMs which break time-reversal symmetry, such as $Y_2Ir_2O_7$ [3], $HgCr_2Se_4$ [17], Co-based magnetic Heusler compounds [40–42], and heterostructures of TIs doped with magnetic impurities [16]. However, so far, none of these proposed magnetic WSMs have been verified in experiments. Some potential reasons may be that the Weyl points in most of these candidate materials are situated far from the Fermi level E_F or the charge carrier density arising from trivial FSs is very large, which makes physical phenomena arising from the Weyl points difficult to observe.

Very recently, a new magnetic WSM was proposed in the layered half-metal $Co_3Sn_2S_2$ [43,44], whose Weyl points were predicted to be situated only 60 meV from the E_F while simultaneously exhibiting a low charge carrier density. As a consequence, the properties of this material that are dominated by the Weyl points should be very easy to detect. Because of the large Berry curvature arising from the Weyl points and nodal lines opened by spin-orbit coupling (SOC), the intrinsic anomalous Hall conductivity (AHC) was predicted to be as large as 1100 S/cm, in full agreement with transport

*ysun@cpfs.mpg.de
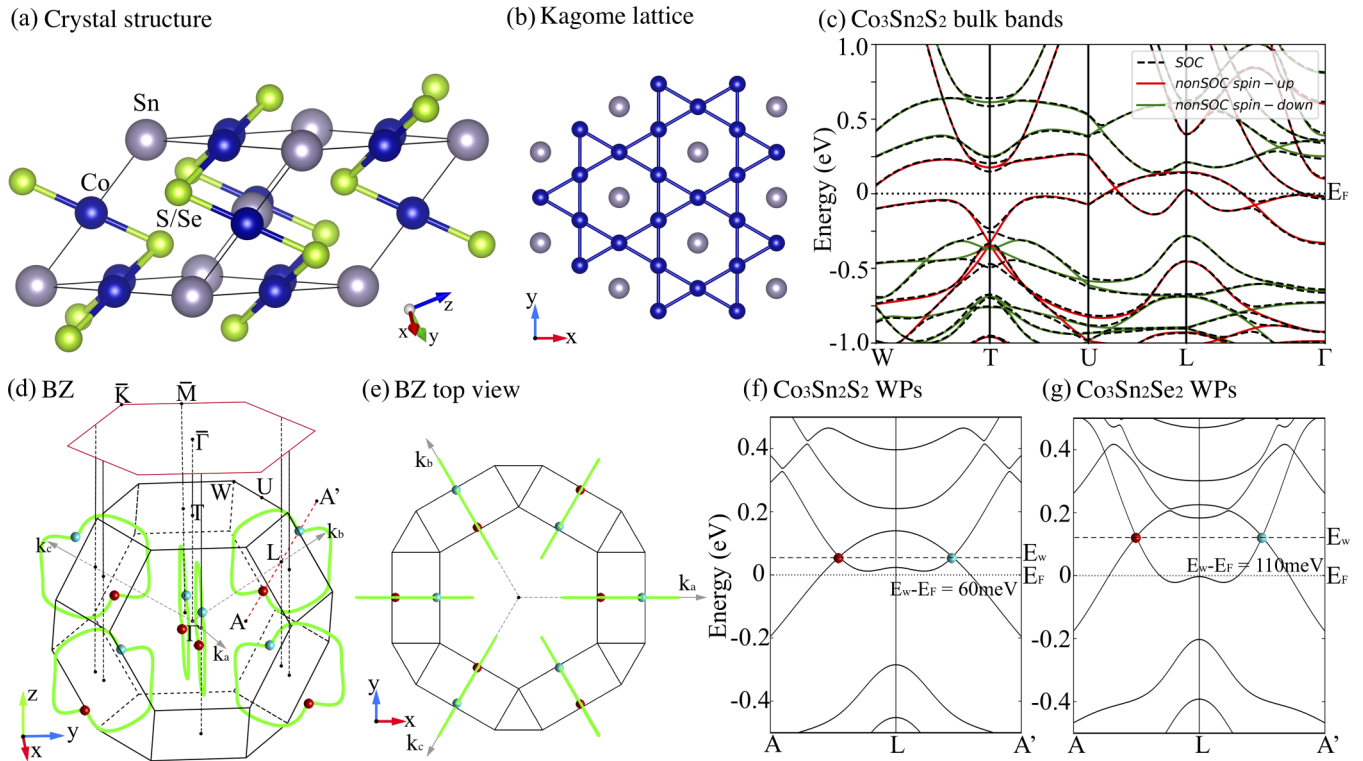
FIG. 1. (a) Rhombohedral lattice structure of $Co_3Sn_2S_2$ and $Co_3Sn_2Se_2$, which exhibit a layered lattice structure in the xy plane. (b) The kagome lattice structure of Co atoms in the xy plane. (c) Band structures of $Co_3Sn_2S_2$, with (black dashed lines) and without (red solid lines for spin up and green solid lines for spin down) SOC. (d) Location of the Weyl points (red and blue represent opposite chiralities) and nodal lines (green) in the 3D Brillouin zone (BZ) and the 2D BZ projected in the (001) direction. (e) Top view along the z direction of BZ with nodal lines and Weyl points. (f) and (g) Energy dispersion along the k path crossing a pair of Weyl points located on the same nodal line for $Co_3Sn_2S_2$ and $Co_3Sn_2Se_2$, respectively. The Fermi level and energy of the Weyl points are labeled E_F and E_W, respectively.

measurements. Moreover, due to the combination of the large AHC and low charge carrier density, the anomalous Hall angle (AHA) was shown to be capable of reaching up to 20%. Therefore, the bulk transport properties provide strong evidence for the existence of Weyl points in $Co_3Sn_2S_2$. In this work, we try to further understand its topological features from the surface point of view through theoretical calculations, which should also be helpful for future surface-state measurements.

II. METHODS

To investigate the electronic and magnetic structures, we applied the Vienna Ab initio Simulation Package (VASP) [45] for the first-principles calculations based on density functional theory (DFT) and chose the generalized gradient approximation of the Perdew-Burke-Ernzerhof functional [46] as the exchange-correlation potential. The cutoff energy was 400 eV, and the k mesh for self-consistent calculation was $10 \times 10 \times 10$. In order to calculate the surface states, we projected the Bloch wave function into maximally localized Wannier functions (MLWFs) [47] derived from the Co $3d$, Sn $5p$, and Se $4p$ orbitals and constructed a tight-binding Hamiltonian from the MLWF overlap matrix. Therefore, the surface states were calculated in a half-infinite boundary condition using the Green's function method [48,49]. Moreover, we also calculated quasiparticle interference (QPI) patterns based on the Fourier-transformed surface local density of states from the Green's

function. The lattice constants are experimentally verified in $Co_3Sn_2S_2$ [43] and only predicted by DFT calculations in $Co_3Sn_2Se_2$ according to Ref. [51].

III. RESULTS

$Co_3Sn_2S_2$ and $Co_3Sn_2Se_2$ exhibit a rhombohedral lattice structure with the space group $R\bar{3}m$ (No. 166) [50,51], which has an inversion center, triple rotation axis, and three mirror planes. The experimental lattice parameters of $Co_3Sn_2S_2$ ($Co_3Sn_2Se_2$) are $a = 5.3757$ Å (5.5635 Å) and $\alpha = 59.91647°$ (58.33°). The Wyckoff sites of atoms are [1/2, 0, 0] for Co, [0, 0, 0] for Sn1, [0.5, 0.5, 0.5] for Sn2, and [n,n,n] for S and Se, where $n = 0.2826$ for S and $n = 0.2864$ for Se. This structure can be viewed as a quasi-two-dimensional (quasi-2D) lattice stacked along the z direction of the Cartesian coordinate system, as shown in Fig. 1(a). The magnetic Co atoms form a kagome lattice in the xy plane, with their magnetic momentum aligned along the z direction as shown in Fig. 1(b), while the Sn atoms assume the central positions of the hexagonal lattice structure. These kagome lattice layers are sandwiched between neighboring S or Se layers and are connected to each other through another Sn layer in the z direction. So far, it is known only that $Co_3Sn_2S_2$ presents a net moment along the z direction. Moreover, there are also some possibilities that each Co atom has a local in-plane (xy plane) component. We have checked some possible magnetic structures with local
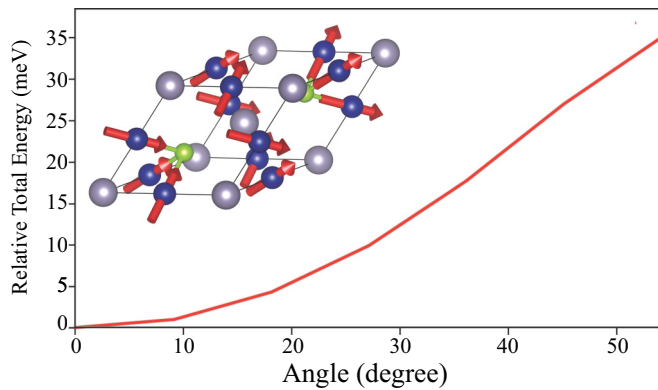
FIG. 2. The change in the total energy with the increasing of the angle between the z axis and magnetic momenta of Co atoms. When the magnetic momenta are parallel to the z axis, it is most stable.

momenta rotating in the plane constructed by the z axis and Co-S bonding and the z component of the local momenta along the positive direction. A comparison of them is given in Fig. 2, from which we can see that the total energy increases along with the increasing of the angle between the local moments and z axis. Although there might be some other possibilities of the magnetic structure, we found that the existence of Weyl points and the anomalous Hall effect are robust as long as the net magnetic moment is along z.

Since $Co_3Sn_2S_2$ and $Co_3Sn_2Se_2$ show very similar electronic band structures and only $Co_3Sn_2S_2$ has been successfully synthesized so far, we will focus on $Co_3Sn_2S_2$ as the example for the detailed analysis. In the absence of SOC, $Co_3Sn_2S_2$ exhibits a half-metallic band structure, where the spin-up channel cuts E_F, while the spin-down channel is insulating, with a band gap of 0.35 eV, as shown in Fig. 1(c). Because of this protection from reflection symmetry, the band inversion of the spin-up states results in linear band crossing in the form of a nodal ring located at the mirror plane. Considering the inversion and C_{3z} rotation symmetries, there are a total of six nodal rings in the whole Brillouin zone (BZ), as indicated in Figs. 1(d) and 1(e). The two linear band crossings indicated at U-L and L-Γ are just two single points of one nodal ring. Moreover, when SOC is taken into consideration, the nodal ring becomes gapped out, and one pair of linear crossings is preserved in the form of Weyl points with opposite topological charges of Chern numbers $+1$ and -1. At the same time, these Weyl points will not locate at the high-symmetry k path. The exact locations of one Weyl point for $Co_3Sn_2S_2$ and one for $Co_3Sn_2Se_2$ are about $(0.313, -0.0866, -0.0866)$ and $(-0.287, 0.106, 0.106)$ in the fraction coordinate of the primitive cell, and the other five Weyl points in the same BZ can also be obtained by inversion and C_{3z} rotation symmetry. In the end, the Weyl points of $Co_3Sn_2S_2$ and $Co_3Sn_2Se_2$ will lie 60 and 110 meV above E_F. Hence, electron doping is preferred for detecting Weyl-point-dominated properties.

A typical feature of WSMs is the nonclosed Fermi arc surface state. For this quasi-2D lattice structure in the xy plane, it is easy to obtain the (001) surface in experiments. So there are two possible cleaving planes: breaking the S-Co bonds or the Sn-S bonds. Because of the atomic separation in the z direction, we found that the bonding between the Sn and S layers is much

weaker, which was confirmed by our total energy calculations. The formation energy required to break the Sn-S bonds is around 2.9 eV per cell. Therefore, the Sn-S bonds are easier to cleave. Thus, we get two different terminations for the cleaved (001) surface, i.e., S and Sn terminals.

In order to check for possible Fermi arc states at E_F, we also analyzed the energy dispersion of the Fermi-arc-related states in energy space. As shown in Fig. 3(b), the Fermi-arc-related bands can extend to $E_F - 0.1$ eV from the energy of Weyl points E_W, which offers a good possibility of detecting the Fermi arcs in the low-energy region. Moreover, we also analyzed the decay of the surface state into the bulk. Here, we pick the sample point K on the surface state [Fig. 3(b)] to calculate the contribution of each unit cell in the slab model with a thickness of 60 unit cells. The result is shown in Fig. 4, from which one can see that at least 30–40 unit cells are needed to obtain the topological surface states. At the same time, the corresponding FS is shown in Fig. 3(c), where the Fermi arcs are located around the corners of the BZ, with the $\bar{K}$ points situated at the center of the three Fermi arcs. For the S-terminated state, most of the Fermi arcs merge into the bulk, making the visible Fermi arc states much shorter than those exhibited for the Sn-terminated states [see Figs. 3(e) and 3(h)]. Moreover, the Fermi-arc-related bands extend to the higher-energy region above the Weyl points, as indicated in Fig. 3(f). Therefore, to observe the Fermi arcs from the S terminal using ARPES, an electron-doped sample and surface electron doping are necessary. However, we note that although potassium doping can be used to achieve small upward shifts in the surface chemical potential [52], this method does not work well in every situation.

Figure 3 shows the surface FSs and energy dispersion corresponding to the two differently terminated surfaces. Fixing the energy at the Weyl points for the Sn-terminated surface, one can easily find the single-surface FS going from one Weyl point to another Weyl point with the opposite chirality, which is the typical expected behavior of Fermi arcs. Taking the C_{3z} rotation symmetry into account, there are three such Fermi arcs in the first BZ, as indicated in Figs. 3(a) and 3(d). Although a small part of the Fermi arc merges into the bulk, the Fermi arc still extends to about 25% of the reciprocal lattice vector, which is sufficiently long to be detected by an ARPES measurement.

Moreover, significantly different from WSMs that exhibit time-reversal symmetry, the surface-state measurements of $Co_3Sn_2S_2$ need to consider the effects of magnetic domains. The size of these domains is typically around the order of a micrometer, which is relatively small in terms of an ARPES measurement. One solution to this problem is to align the magnetic moments along a particular direction by applying an external field. However, this is not generally feasible for ARPES measurements. Alternatively, a surface-sensitive STM probe can gather enough information within the range of one domain, provided that the surface is sufficiently smooth, since the sample surface can be scanned atom by atom. Furthermore, STM measurements yield another advantage by allowing us to measure the surface states at energies above E_F. Since the magnitude of the dI/dV spectrum is proportional to the surface local density of states, the intensity of elastically scattering electrons from surface defects can reveal the resulting QPI
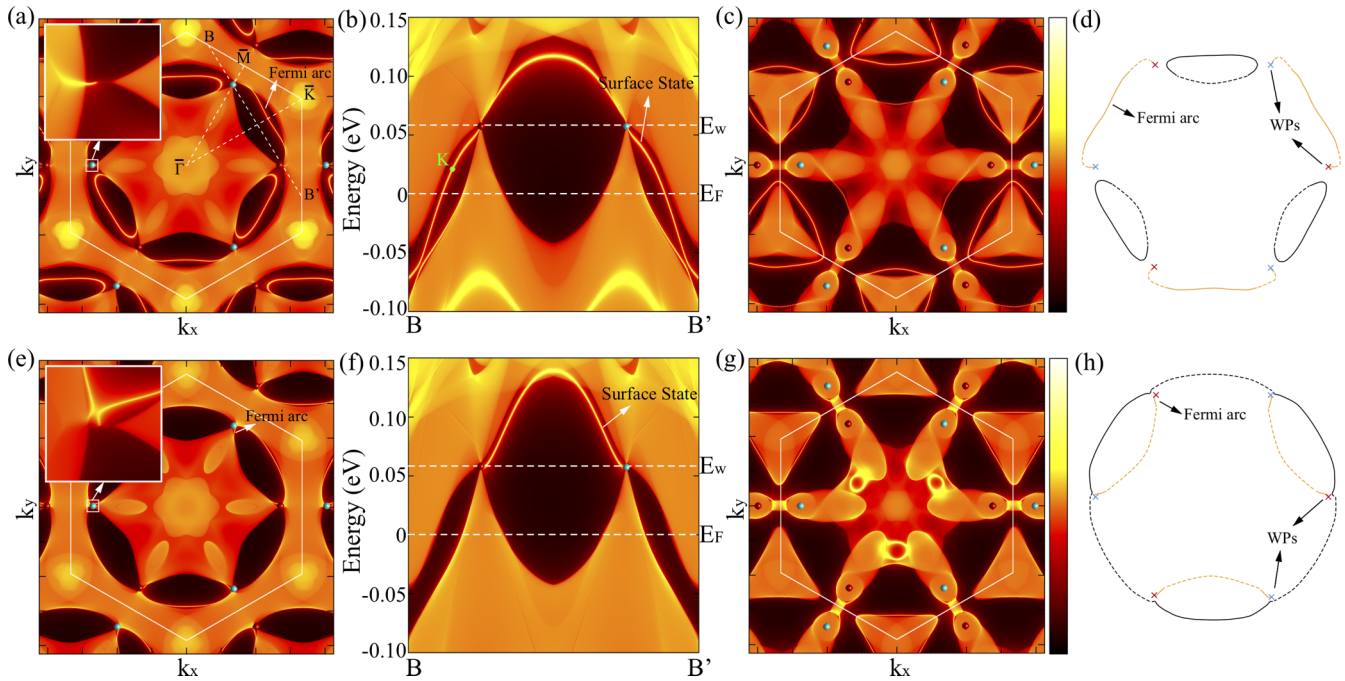
FIG. 3. The (001) surface states of $Co_3Sn_2S_2$ for S and Sn terminals. (a) Sn-terminated surface FS with energy fixed at the Weyl points. (b) Energy dispersion for the Sn-terminated surface along a k path crossing a pair of Weyl points connected by a Fermi arc. (c) Sn-terminated surface FS at the charge-neutral point. (d) Schematic diagram of the FS distribution on the Sn-terminated surface. (e) S-terminated surface FS with energy fixed at the Weyl points. (f) Surface band structure for S-terminated states taken along the same direction as that in (b). (g) S-terminated surface FS at the Fermi energy E_F. (h) Schematic diagram of the FS distribution on the S-terminated surface. The color bars for (a)–(c) and (e)–(g) demonstrate the intensity of states. Light (dark) color demonstrates the occupied (unoccupied) states. The dashed curves in (d) and (h) represent surface states that merge into the bulk. The Fermi arcs and trivial FSs are shown in yellow and black, respectively.

pattern. The quantum interference between initial and final states (k_i and k_f) at a constant energy results in a standard wave pattern indexed by a vector $q = k_f - k_i$.

In order to simulate such an STM measurement, we calculated the QPI from the surface local density of states [53–55]. In contrast to ARPES measurements, the QPI in STM is much more sensitive to the surface states, where the effects of k_z are almost negligible. In this sense, we can justify the
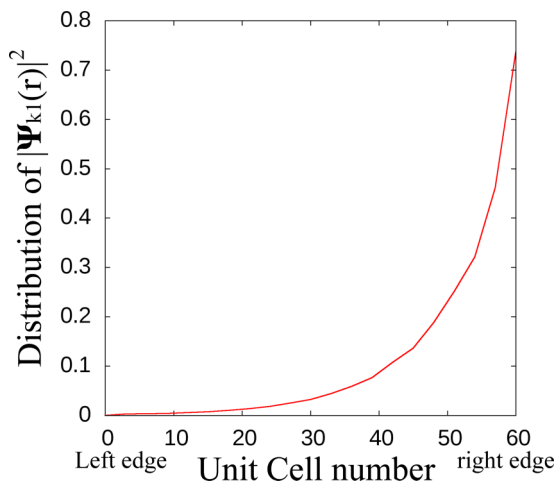
FIG. 4. The decay of the surface state into the bulk. The wave function at the sample point K in Fig. 3(b) on the surface state shows its decay into bulk as a function of the number of unit cells. The penetration depth is about 30–40 unit cells.

exclusion of the bulk projected states in our QPI calculations. Moreover, owing to the magnetic polarization in $Co_3Sn_2S_2$, the spins will be oriented along the z direction with small in-plane components, and the QPI pattern is thus decided by the joint density of states (JDOS) without considering further spin selection rules.

Figure 5 shows the resulting QPI pattern for the Sn terminal with an energy fixed at the Weyl points. In order to accurately simulate the scattering, we considered only the states arising from the surface, as indicated in Fig. 5(a). Besides the Fermi arcs, other trivial FS states arising from the dangling bond also exist, but they partly merge into the bulk, which appears alternately with the Fermi arc around the k_z axis. According to the symmetry of the FSs, there are thus six independent scattering vectors for each Fermi arc, three arising from arc-arc scattering and the other three arising from scattering between the Fermi arcs and the trivial FS, which is shown in Fig. 5(a).

Further details regarding the contributions of the different scattering intensities are presented in Figs. 5(d)–5(i). As highlighted by the rectangle in Fig. 5(a), the Fermi arc appears as a nearly straight line at E_F. As a consequence, the intensity of the JDOS from intra-arc scattering forms the G_0-point centered line, which is indicated by q_1 in Fig. 5(d). In contrast, the JDOS patterns arising from scatterings between the Fermi arcs and trivial FSs are relatively wide due to the curvature of the trivial FS, as shown in Figs. 5(g)–5(i), with the corresponding wave vectors labeled q_4, q_5, and q_6. To distinguish arc-related scatterings from the full QPI, we combined all the Fermi-arc-related JDOSs in Fig. 5(c), which includes the intra-arc
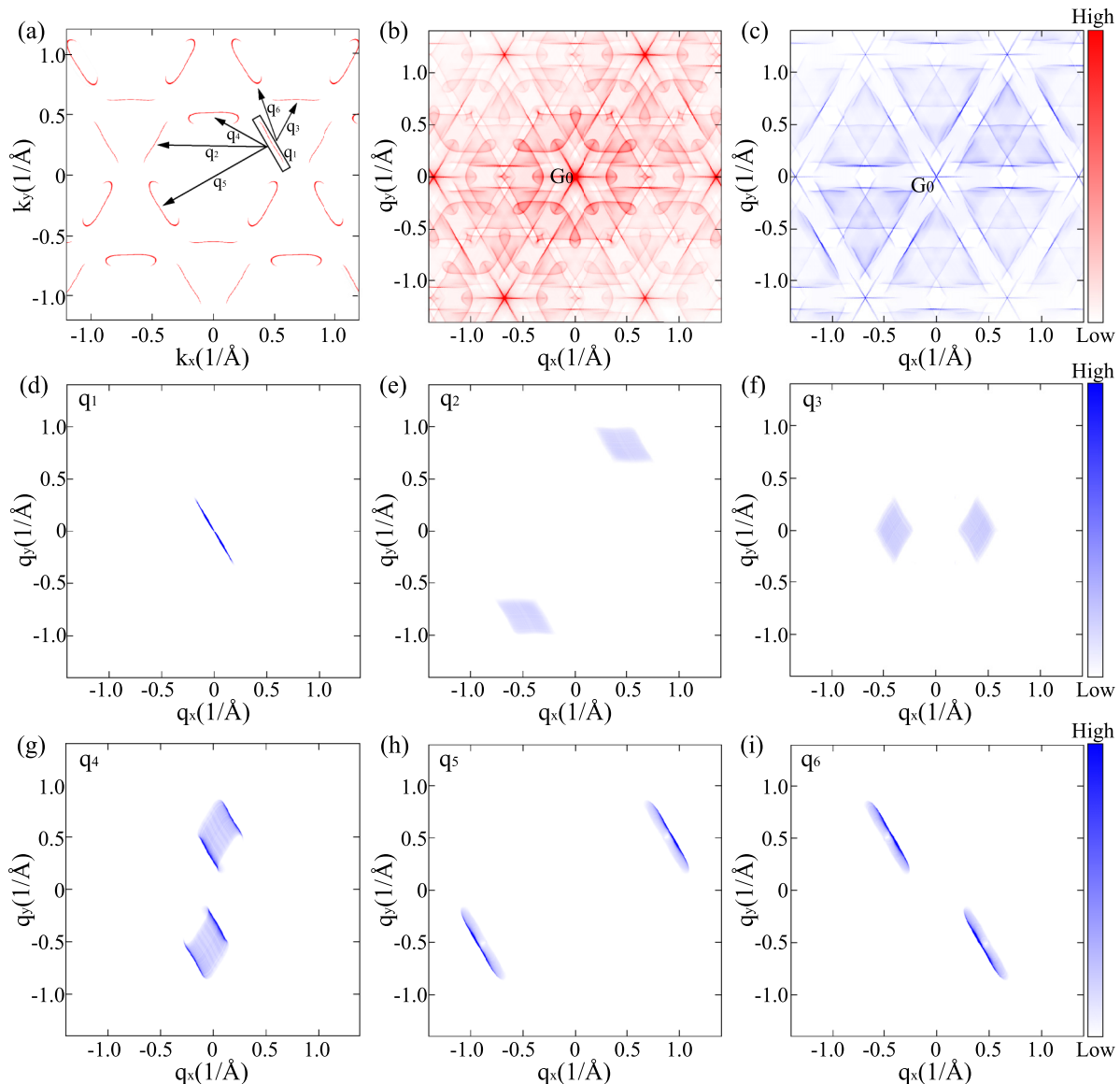
FIG. 5. QPI patterns for an Sn-terminated surface. (a) Surface FSs without those that merge into the bulk states. The independent scattering vectors q_1-q_6 are labeled with arrows. (b) QPI patterns taking contributions from all possible scatterings into account. (c) QPI patterns considering only Fermi-arc-related scatterings. (d) The intra-arc scattering of a nontrivial Fermi arc. (e) and (f) Specified interarc scattering patterns between two nontrivial Fermi arcs. (g)–(i) Details of the interarc scattering between a nontrivial Fermi arc and a trivial FS.

scattering of Fermi arcs, the interarc scattering between two Fermi arcs, and the interarc scattering between Fermi arcs and trivial FSs. Compared with the full QPI, the arc-related QPI mainly dominates the six triangular regions near the central point G_0.

In contrast, the Fermi arc is very short for the S-terminated surface due to strong mixing between its central part and the bulk states. Figure 6(a) displays all the visible FSs, which include part of the Fermi arcs and part of the trivial FS that is not merged into the bulk. As a result of the short visible Fermi arc, arc-arc scattering contributes only a marginal amount to the overall QPI pattern. As indicated in Figs. 6(a) and 6(d), q_1, which represents arc-arc scattering from the same Fermi arc, yields only a tiny contribution to the whole q space: one contribution located around the center of the BZ and two others at $(q_x, q_y) = (\pm 0.5, q_y)$.

In addition to this arc-arc scattering, there are five other independent arc-related q vectors, as indicated in Fig. 6(a). For convenience, we may view the two nearby broken Fermi arcs and trivial FSs as a single local FS due to the short distance between them, as marked by the black rectangle in Fig. 6(a). Then, using one visible part of the Fermi arc as the center, we are able to analyze other arc-related scattering channels, which can be classified into five groups. The indicated q_2 channel corresponds to the closest scattering between the Fermi arc and the trivial FS, which results in an S-shaped pattern, as shown in Fig. 6(d). After taking the rotation and mirror symmetries into account, the resulting intensity pattern yields a G_0-centered pattern with three ∞-shaped branches, as shown in Fig. 6(c). In addition to the ∞-shaped pattern, the intensities of the other four scattering channels also form some nonclosed patterns located relatively far away from G_0
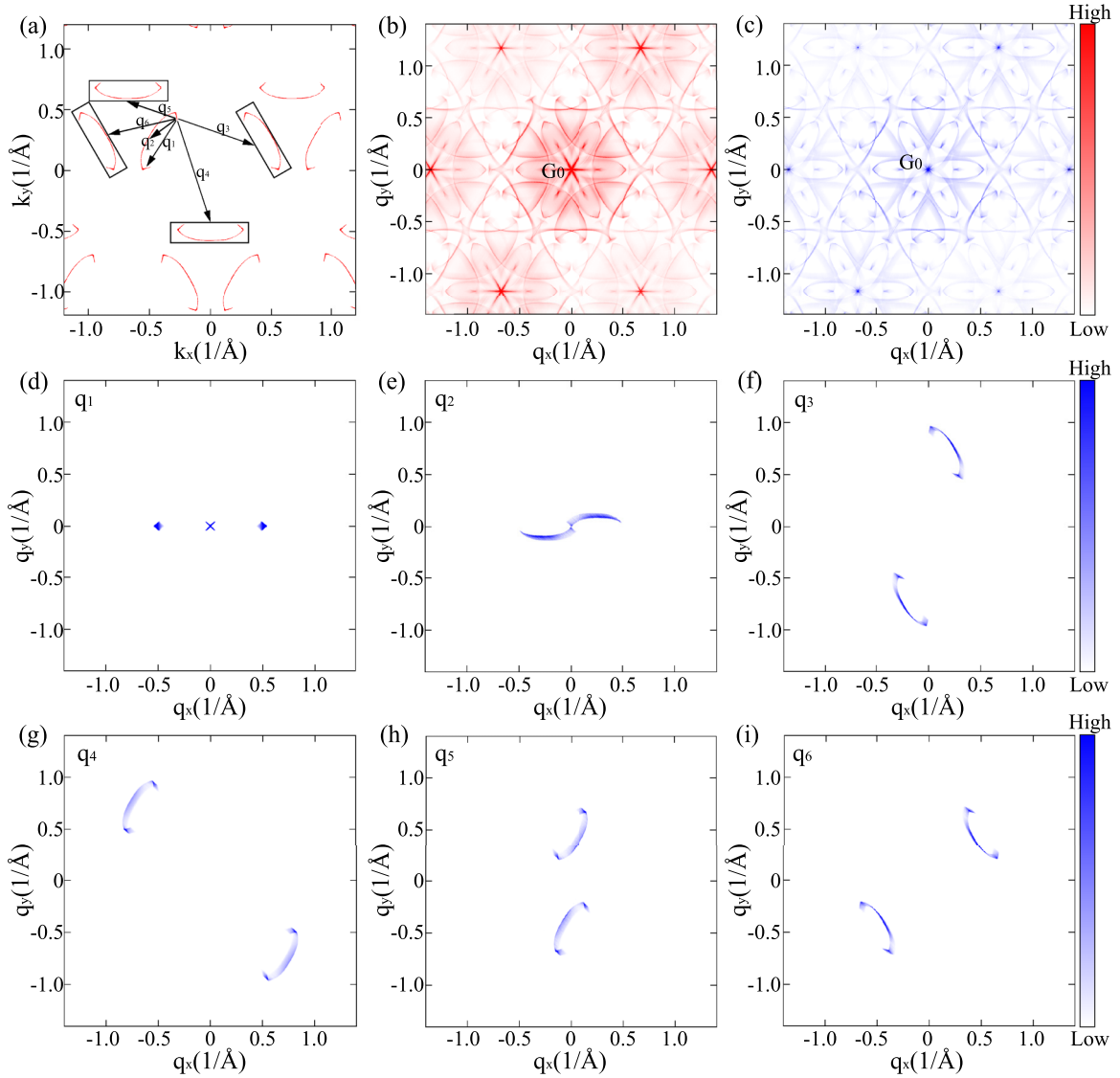
FIG. 6. QPI patterns for an S-terminated surface. (a) Surface FSs excluding parts that merge into the bulk states. The six Fermi-arc-related independent scattering vectors are labeled q_1-q_6. (b) Full QPI pattern taking all possible surface-state scattering channels into account. (c) QPI pattern considering only the scattering from the nontrivial Fermi arcs. (d) Intensity of the q_1 arc-arc scattering. (e)–(i) Intensity distributions of the five independent Fermi-arc-related interarc scattering q_2-q_6.

[see Figs. 6(f)–6(i)]. Considering all kinds of arc-related scattering, the QPI pattern shown in Fig. 6(c) can be obtained.

IV. SUMMARY

We theoretically studied the topological surface Fermi arc states in the magnetic Weyl semimetals $Co_3Sn_2S_2$ and $Co_3Sn_2Se_2$. The cleaved (001) surfaces have two possible terminations, the Sn terminal and the S/Se terminal, due to the weak chemical bonding between the Sn and S/Se layers. Fixing the energy at the Weyl points, the Fermi arcs are shown to be capable of extending to around 25% of the reciprocal lattice vector in Sn-terminated states. Owing to the strong dispersion of the nontrivial surface state which extends from $E_F - 0.1$ eV to $E_F + E_W$, the large energy window provides a good possibility of observing Fermi arc states in ARPES

measurements. In contrast, the Fermi arcs for S/Se-terminated surfaces exist only above E_F and are relatively short due to mixing of the surface and bulk states. Furthermore, we also simulated STM measurements of the differently terminated surfaces. These results will be helpful for a clear understanding of the surface Fermi arcs in these two magnetic WSMs.

[1] X.-L. Qi and S.-C. Zhang, Rev. Mod. Phys. **83**, 1057 (2011).

[2] M. Z. Hasan and C. L. Kane, Rev. Mod. Phys. **82**, 3045 (2010).

[3] X. G. Wan, A. M. Turner, A. Vishwanath, and S. Y. Savrasov, Phys. Rev. B **83**, 205101 (2011).

[4] A. A. Burkov, M. D. Hook, and L. Balents, Phys. Rev. B **84**, 235126 (2011).

[5] S. M. Young, S. Zaheer, J. C. Y. Teo, C. L. Kane, E. J. Mele, and A. M. Rappe, Phys. Rev. Lett. **108**, 140405 (2012).

[6] Z. Wang, Y. Sun, X.-Q. Chen, C. Franchini, G. Xu, H. Weng, X. Dai, and Z. Fang, Phys. Rev. B **85**, 195320 (2012).

[7] H. Weng, C. Fang, Z. Fang, B. A. Bernevig, and X. Dai, Phys. Rev. X **5**, 011029 (2015).

[8] M. Zeng, C. Fang, G. Chang, Y.-A. Chen, T. Hsieh, A. Bansil, H. Lin, and L. Fu, arXiv:1504.03492.

[9] J.-P. Sun, D. Zhang, and K. Chang, Phys. Rev. B **96**, 045121 (2017).

[10] J.-P. Sun, D. Zhang, and K. Chang, Chin. Phys. Lett. **34**, 027102 (2017).

[11] X. Huang, L. Zhao, Y. Long, P. Wang, D. Chen, Z. Yang, H. Liang, M. Xue, H. Weng, Z. Fang, X. Dai, and G. Chen, Phys. Rev. X **5**, 031023 (2015).

[12] C.-L. Zhang, S.-Y. Xu, I. Belopolski, Z. Yuan, Z. Lin, B. Tong, G. Bian, N. Alidoust, C.-C. Lee, S.-M. Huang, T.-R. Chang, G. Chang, C.-H. Hsu, H.-T. Jeng, M. Neupane, D. S. Sanchez, H. Zheng, J. Wang, H. Lin, C. Zhang, H.-Z. Lu, S.-Q. Shen, T. Neupert, M. Z. Hasan, and S. Jia, Nat. Commun. **7**, 10735 (2016).

[13] Z. Wang, Y. Zheng, Z. Shen, Y. Lu, H. Fang, F. Sheng, Y. Zhou, X. Yang, Y. Li, C. Feng, and Z.-A. Xu, Phys. Rev. B **93**, 121112(R) (2016).

[14] A. C. Niemann, J. Gooth, S.-C. Wu, S. Bäßler, P. Sergelius, R. Hühne, B. Rellinghaus, C. Shekhar, V. Suß, M. Schmidt, C. Felser, B. Yan, and K. Nielsch, Sci. Rep. **7**, 43394 (2017).

[15] J. Gooth, A. C. Niemann, T. Meng, A. G. Grushin, K. Landsteiner, B. Gotsmann, F. Menges, M. Schmidt, C. Shekhar, V. Sueß, R. Huehne, B. Rellinghaus, C. Felser, B. Yan, and K. Nielsch, Nature **547**, 324 (2017).

[16] A. A. Burkov and L. Balents, Phys. Rev. Lett. **107**, 127205 (2011).

[17] G. Xu, H. Weng, Z. Wang, X. Dai, and Z. Fang, Phys. Rev. Lett. **107**, 186806 (2011).

[18] Y. Sun, Y. Zhang, C. Felser, and B. Yan, Phys. Rev. Lett. **117**, 146403 (2016).

[19] C. Shekhar, A. K. Nayak, Y. Sun, M. Schmidt, M. Nicklas, I. Leermakers, U. Zeitler, Y. Skourski, J. Wosnitza, Z. Liu, Y. Chen, W. Schnelle, H. Borrmann, Y. Grin, C. Felser, and B. Yan, Nat. Phys. **11**, 645 (2015).

[20] N. J. Ghimire, Y. Luo, M. Neupane, D. J. Williams, E. D. Bauer, and F. Ronning, J. Phys.: Condens. Matter **27**, 152201 (2015).

[21] Y. Luo, N. J. Ghimire, M. Wartenbe, H. Choi, M. Neupane, R. D. McDonald, E. D. Bauer, J. Zhu, J. D. Thompson, and F. Ronning, Phys. Rev. B **92**, 205134 (2015).

[22] P. J. W. Moll, A. C. Potter, N. L. Nair, B. J. Ramshaw, K. A. Modic, S. Riggs, B. Zeng, N. J. Ghimire, E. D. Bauer, R. Kealhofer, F. Ronning, and J. G. Analytis, Nat. Commun. **7**, 12492 (2016).

[23] S.-Y. Xu, I. Belopolski, N. Alidoust, M. Neupane, G. Bian, C. Zhang, R. Sankar, G. Chang, Y. Zhujun, C.-C. Lee, S.-M. Huang, H. Zheng, J. Ma, D. S. Sanchez, B. Wang, A. Bansil, F. Chou, P. P. Shibayev, H. Lin, S. Jia, and M. Z. Hasan, Science **349**, 613 (2015).

[24] B. Q. Lv, H. M. Weng, B. B. Fu, X. P. Wang, H. Miao, J. Ma, P. Richard, X. C. Huang, L. X. Zhao, G. F. Chen, Z. Fang, X. Dai, T. Qian, and H. Ding, Phys. Rev. X **5**, 031013 (2015).

[25] L. X. Yang, Z. K. Liu, Y. Sun, H. Peng, H. F. Yang, T. Zhang, B. Zhou, Y. Zhang, Y. F. Guo, M. Rahn, D. Prabhakaran, Z. Hussain, S. K. Mo, C. Felser, B. Yan, and Y. L. Chen, Nat. Phys. **11**, 728 (2015).

[26] Z. K. Liu, L. X. Yang, Y. Sun, T. Zhang, H. Peng, H. F. Yang, C. Chen, Y. Zhang, Y. F. Guo, D. Prabhakaran, M. Schmidt, Z. Hussain, S.-K. Mo, C. Felser, B. Yan, and Y. L. Chen, Nat. Mater. **15**, 27 (2015).

[27] S.-Y. Xu, N. Alidoust, I. Belopolski, Z. Yuan, G. Bian, T.-R. Chang, H. Zheng, V. N. Strocov, D. S. Sanchez, G. Chang, C. Zhang, D. Mou, Y. Wu, L. Huang, C.-C. Lee, S.-M. Huang, B. Wang, A. Bansil, H.-T. Jeng, T. Neupert, A. Kaminski, H. Lin, S. J. Jia, and M. Z. Hasan, Nat. Phys. **11**, 748 (2015).

[28] I. Belopolski, S.-Y. Xu, D. S. Sanchez, G. Chang, C. Guo, M. Neupane, H. Zheng, C.-C. Lee, S.-M. Huang, G. Bian, N. Alidoust, T.-R. Chang, B. K. Wang, X. Zhang, A. Bansil, H.-T. Jeng, H. Lin, S. Jia, and M. Z. Hasan, Phys. Rev. Lett. **116**, 066802 (2016).

[29] N. Xu, H. M. Weng, B. Q. Lv, C. E. Matt, J. Park, F. Bisti, V. N. Strocov, D. Gawryluk, E. Pomjakushina, K. Conder, N. C. Plumb, M. Radovic, G. Autès, O. V. Yazyev, Z. Fang, X. Dai, T. Qian, J. Mesot, H. Ding, and M. Shi, Nat. Commun. **7**, 11006 (2016).

[30] S. Souma, Z. Wang, H. Kotaka, T. Sato, K. Nakayama, Y. Tanaka, H. Kimizuka, T. Takahashi, K. Yamauchi, T. Oguchi, K. Segawa, and Y. Ando, Phys. Rev. B **93**, 161112 (2016).

[31] H. Inoue, A. Gyenis, Z. Wang, J. Li, S. W. Oh, S. Jiang, N. Ni, B. A. Bernevig, and A. Yazdani, Science **351**, 1184 (2016).

[32] R. Batabyal, N. Morali, N. Avraham, Y. Sun, M. Schmidt, C. Felser, A. Stern, B. Yan, and H. Beidenkopf, Sci. Adv. **2**, e1600709 (2016).

[33] H. Zheng, S.-Y. Xu, G. Bian, C. Guo, G. Chang, D. S. Sanchez, I. Belopolski, C.-C. Lee, S.-M. Huang, X. Zhang, R. Sankar, N. Alidoust, T.-R. Chang, F. Wu, T. Neupert, F. Chou, H.-T. Jeng, N. Yao, A. Bansil, S. Jia, H. Lin, and M. Z. Hasan, ACS Nano **10**, 1378 (2016).

[34] A. A. Soluyanov, D. Gresch, Z. Wang, Q. Wu, M. Troyer, X. Dai, and B. A. Bernevig, Nature (London) **527**, 495 (2015).

[35] Y. Sun, S. C. Wu, M. N. Ali, C. Felser, and B. Yan, Phys. Rev. B **92**, 161107(R) (2015).

[36] K. Deng, G. Wan, P. Deng, K. Zhang, S. Ding, E. Wang, M. Yan, H. Huang, H. Zhang, Z. Xu, J. Denlinger, A. Fedorov, H. Yang,

W. Duan, H. Yao, Y. Wu, S. Fan, H. Zhang, X. Chen, and S. Zhou, Nat. Phys. **12**, 1105 (2016).

[37] J. Jiang, Z. K. Liu, Y. Sun, H. F. Yang, R. Rajamathi, Y. P. Qi, L. X. Yang, C. Chen, H. Peng, C. C. Hwang, S. Z. Sun, S.-K. Mo, I. Vobornik, J. Fujii, S. Parkin, C. Felser, B. H. Yan, and Y. L. Chen, Nat. Commun. **8**, 13973 (2017).

[38] A. Liang, J. Huang, S. Nie, Y. Ding, Q. Gao, C. Hu, S. He, Y. Zhang, C. Wang, B. Shen, J. Liu, P. Ai, L. Yu, X. Sun, W. Zhao, S. Lv, D. Liu, C. Li, Y. Zhang, Y. Hu, Y. Xu, L. Zhao, G. Liu, Z. Mao, X. Jia, F. Zhang, S. Zhang, F. Yang, Z. Wang, Q. Peng, H. Weng, X. Dai, Z. Fang, Z. Xu, C. Chen, and X. J. Zhou, arXiv:1604.01706.

[39] L. Huang, T. M. McCormick, M. Ochi, Z. Zhao, M.-T. Suzuki, R. Arita, Y. Wu, D. Mou, H. Cao, J. Yan, N. Trivedi, and A. Kaminski, Nat. Mater. **15**, 1155 (2016).

[40] Z. W. Wang, M. G. Vergniory, S. Kushwaha, M. Hirschberger, and E. V. Chulkov, Phys. Rev. Lett. **117**, 236401 (2016).

[41] T.-R. Chang, S.-Y. Xu, G. Chang, C.-C. Lee, S.-M. Huang, B. Wang, G. Bian, H. Zheng, D. S. Sanchez, I. Belopolski, N. Alidoust, M. Neupane, A. Bansil, H.-T. Jeng, H. Lin, and M. Z. Hasan, Nat. Commun. **7**, 10639 (2016).

[42] J. Kubler and C. Felser, Europhys. Lett. **114**, 47005 (2016).

[43] E. Liu, Y. Sun, L. Müechler, A. Sun, L. Jiao, J. Kroder, V. Süß, H. Borrmann, W. Wang, W. Schnelle, S. Wirth, S. T. B. Goennenwein, and C. Felser, arXiv:1712.06722.

[44] Q. Wang, Y. Xu, R. Lou, Z. Liu, M. Li, Y. Huang, D. Shen, H. Weng, S. Wang, and H. Lei, arXiv:1712.09947.

[45] G. Kresse and J. Furthmüller, Phys. Rev. B **54**, 11169 (1996).

[46] J. P. Perdew, K. Burke, and M. Ernzerhof, Phys. Rev. Lett. **77**, 3865 (1996).

[47] A. A. Mostofi, J. R. Yates, Y.-S. Lee, I. Souza, D. Vanderbilt, and N. Marzari, Comput. Phys. Commun. **178**, 685 (2008).

[48] M. P. L. Sancho, J. M. L. Sancho, and J. Rubio, J. Phys. F **14** 1205 (1984).

[49] M. P. L. Sancho, J. M. L. Sancho, and J. Rubio, J. Phys. F **15** 851 (1985).

[50] R. Weihrich, W. Yan, J. Rothballer, P. Peter, S. M. Rommel, S. Haumann, F. Winter, C. Schwickert, and R. Pöttgen, Dalton Trans. **44**, 15855 (2015).

[51] Y. Sakai, Y. Kamihara, and M. Matoba, Phys. Status Solidi C **10**, 1130 (2013).

[52] M. A. Hossain, J. D. F. Mottershead, D. Fournier, A. Bostwick, J. L. Mcchesney, E. Rotenberg, R. Liang, W. N. Hardy, G. A. Sawatzky, I. S. Elfimov, D. A. Bonn, and A. Damascelli, Nat. Phys. **4**, 527 (2008).

[53] P. Hosur, Phys. Rev. B **86**, 195102 (2012).

[54] J. S. Hofmann, R. Queiroz, and A. P. Schnyder, Phys. Rev. B **88**, 134505 (2013).

[55] S. Kourtis, J. Li, Z. Wang, A. Yazdani, and B. A. Bernevig, Phys. Rev. B **93**, 041109 (2016).